Tomography of (2, 1) and (3, 2) magnetic island structures on Tokamak Fusion Test Reactor

Y. Nagayama
National Institute for Fusion Science, Nagoya 464-01, Japan

G. Taylor, E. D. Fredrickson, R. V. Budny, A. C. Janos, D. K. Mansfield, K. M. McGuire, and M. Yamada
Plasma Physics Laboratory, Princeton University, Princeton, New Jersey 08543

High-resolution electron cyclotron emission (ECE) image reconstruction has been used to observe $(m,n) = (2,1)$ and $(3, 2)$ island structures on Tokamak Fusion Test Reactor [Plasma Phys. Controlled. Fusion **33**, 1509 (1991)], where m and n are the poloidal and the toroidal mode number, respectively. The observed island structure is compared with other diagnostics, such as soft x-ray tomography and magnetic measurements. A cold elliptic island is observed after lithium pellet injection. Evidence for the enhancement of the heat transfer due to the island is observed. A relaxation phenomenon due to the $m = 2$ mode is newly observed in Ohmic plasmas. © *1996 American Institute of Physics.* [S1070-664X(96)02107-6]

I. INTRODUCTION

The concept of the magnetic island is one of the most important results of magnetohyrodynamic (MHD) theory and successfully explains the Mirnov oscillation.[1] Magnetic islands may be crescent-shaped and flat as described in text books on MHD physics.[2,3] The rotational soft x-ray tomography technique has been employed to observe the $(m,n) = (2, 1)$ island structure,[4,5] but the quality of the observed $(2, 1)$ island structure has been rather poor, where m is the poloidal mode number and n is the toroidal mode number. In most cases, the $(2, 1)$ mode sits on a low soft x-ray emission region and the $(2, 1)$ mode is accompanied by the $(1, 1)$ mode,[6] so the detected soft x-ray, which is a line integral of soft x-ray emission along the viewing line, is a mixture of the strong $(1, 1)$ mode and the weak $(2, 1)$ mode. These two modes have different helicities. The principle of the rotational tomography is as follows: (1) mode structure, which has a helical symmetry, rigidly rotates in the toroidal direction; (2) the toroidal rotation of a helical symmetric structure is equivalent to the poloidal rotation. The weak point is that mode structures with different helicities cannot be reconstructed. Therefore, rotational soft x-ray tomography of the $(2, 1)$ mode is often impossible.

Recently, electron cyclotron emission (ECE) imaging has been developed in the Tokamak Fusion Test Reactor (TFTR).[7–9] Since the ECE provides a local measurement of the electron temperature and the contours of the electron temperature best represent the flux surfaces, ECE reconstruction is a powerful method for the measurement of the island structure. Since the different modes locate different position, ECE image of a mode structure can be reconstructed separately. Using ECE reconstruction, the $(1, 1)$ mode and $(2, 1)$ mode can be separately detected. So, the island size of the $(2, 1)$ mode can be obtained using ECE imaging. The reconstruction technique and its reliability are discussed in a previous paper.[7,9] Since we have data from both in board side and out board side, the Shafranov shift, the ballooning effect, and other in-out asymmetries are taken into account. The main conclusions are as follows: (1) the MHD mode rotates rigidly even if the impurity rotation velocity varies in the radial position; (2) the reconstruction error is small if the crash time is longer than two rotational periods.

This paper precisely documents the island structures of the $(2, 1)$ and $(3, 2)$ modes. First, the ECE reconstruction is compared with other diagnostics (soft x-ray tomography and electron density tomography). Second, the structure of a $(2, 1)$ island, which is caused by a β collapse[10,11] or pellet injection, will be described. Third, the $(3, 2)$ mode structure and its effect on transport during the β degradation will be discussed. Fourth, the temperature profile relaxation due to the $(2, 1)$ mode will be presented. The magnetic signals will be presented in all examples. Finally, the comparison between the ECE measurement and the magnetic measurement will be summarized.

II. EXPERIMENTAL SETUP

The electron temperature profile on the mid-plane of the plasma is measured with a 20 channel grating polychromator.[12] The polychromator data is cross-calibrated to a Michelson interferometer;[13] although the uncertainty of absolute temperature is 5%–10%, the point-to-point relative error is less than 2%. The data are collected with a 2 μs time resolution and a major radial coverage of $R = 220$–340 cm, with a channel separation of 6 cm (each channel has a radial resolution of 3 cm). The poloidal resolution of the reconstructed image is 11°. The data from the inside and outside major radii are used for a full rotation, and an interpolation between both sides is carried out, so that the time resolution is better than the period of a half rotation.[7]

In TFTR, two soft x-ray cameras separated by 75° view the plasma through 125 μm thick beryllium filters, one vertically and the other horizontally. The cameras have 20 and 60 silicon-diode detectors, respectively.[14,15] With this filter, the detector energy range is 3 keV to 15 keV (sensitivity greater than 50% of its maximum).[14] The ECE and soft x-ray data are synchronously sampled every 2 μs. Soft x-ray to-
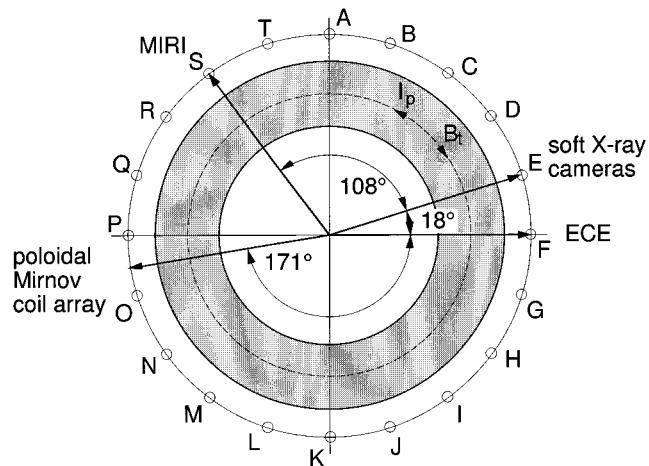
FIG. 1. Toroidal location of ECE, soft x-ray camera, MIRI, and Mirnov coil array.

FIG. 2. (a) Time evolution of soft x-ray, central plasma density (n_{e0}), ICRF heating power, and poloidal beta (β_p). (b) ECE signals in the case of pellet injection. (c) Time evolution of perturbation on the electron temperature profile in the plasma with deuterium pellet injection. The dotted lines show rational surfaces. (d) The q profile being estimated by the transport code SNAP.[18]

mography is performed with a Fourier-Bessel expansion technique.[16] The x-ray emission is characterized by a Fourier series of order 7 and a Bessel function expansions of order 10. The data are taken during a quarter rotation using the two cameras, so the time resolution is 17 μs. The effective radial resolution is 9 cm and the poloidal resolution is 13°.

A 10 channel methanol laser interferometer system (MIRI) is used for electron density measurements on TFTR.[17] The laser chords pass vertically, and the data are sampled every 10 μs. The toroidal location of those diagnostics (ECE, soft x-ray, and MIRI) and a Mirnov coil array is shown in Fig. 1. The poloidal magnetic field fluctuation is measured by the Mirnov coil array. Also other Mirnov coils are distributed toroidally. Using the Mirnov coil system, the toroidal and poloidal mode number of the magnetic fluctuation can be identified. Using the rotational tomography technique,[16] the two dimensional (2-D) cross-section of the electron density can be obtained.

III. (2, 1) MODES

A. Image reconstruction of ECE perturbation

The contour plot of the perturbation amplitude provides a visual representation of the instabilities and facilitates identification of the location and relative spatial intensity of the oscillations.[8] The ECE (perturbation) $\tilde{f}(t)$ is defined as

$$\tilde{f}(t) = f(t) - \frac{1}{T}\int_{t-T/2}^{t+T/2} f(t)dt, \qquad (1)$$

where $f(t)$ is the ECE signal, and T is a one cycle period of the dominant mode. Theoretically, the island structure is created due to the reconnection at the X-point, which is on the rational surface. Therefore, the theoretically expected (2, 1) island is crescent-shaped. In the ECE reconstruction, two crescent-shaped (2, 1) islands are seen as expected. The rational surface is at the boundary of the positive and negative perturbation domains. The reason is as follows. The temperature in the island is basically identical to the temperature at
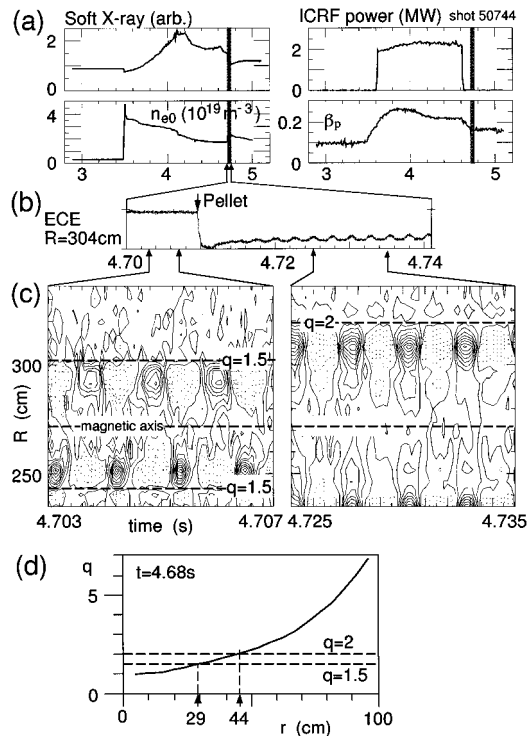
the X-point. The isothermal surface with the X-point is the rational surface. Since the plasma rotates along the flux surface, the temperature on the rational surface does not change, while temperature inside and outside the rational surface changes. Therefore, the rational surface is observed as an isotherm in the ECE (perturbation) reconstruction.

ECE imaging of the perturbed temperature can determine the rational surface. This technique can be used to examine the effect on the current profile due to the pellet injection. Figure 2 shows time evolution of the contour plot of the perturbed electron temperature after the deuterium pellet injection into the plasma, which has a (3, 2) mode. The (2, 1) mode is enhanced after the pellet injection. Figure 2 also shows the q-profile, which is estimated before the pellet injection from the profile measurements of temperature, density, and radiation using the one dimensional (1-D) steady-state transport analysis code SNAP.[18] The location of the observed $q=1.5$ surface before the pellet injection is $r=30$ cm, which is similar to the SNAP estimation $r=29$ cm. The location of the observed $q=2$ surface after the pellet injection is $r=47$ cm, which is similar to the SNAP estimation $r=44$ cm. This result shows that the location of the rational surfaces is roughly similar before and after the pellet injection. Due to the pellet injection, the electron temperature drops very quickly, but the diffusion time of the current profile may be much longer. Therefore the current profile may not change on the time scale of the pellet injection.
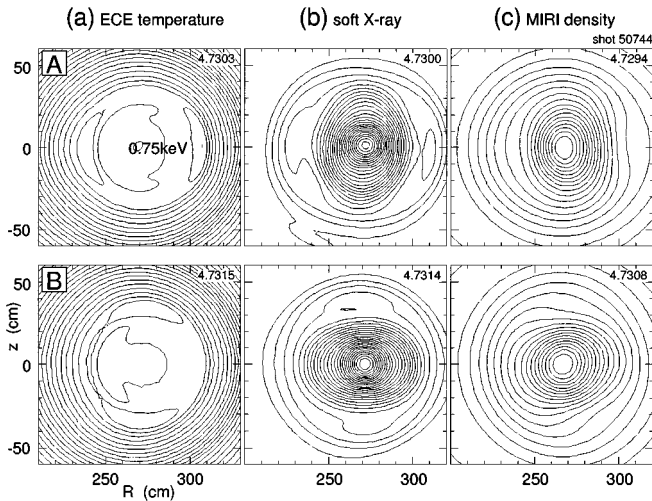
Nagayama *et al.*

FIG. 3. (a) Contour plot of electron temperature profile showing the (2, 1) mode in the Ohmic plasma with deuterium pellet injection. The contour step size is 30 eV. (b) The soft x-ray tomography. (c) The electron density tomography of a (2, 1) mode, which is enhanced after the deuterium pellet injection. The capital letters on the left of the figures correspond to the alphabets in Fig. 4.

B. Observation of islands by different diagnostics

Figure 3 shows (2,1) islands, which are measured using three different diagnostics, the ECE image reconstruction, the soft x-ray tomography, and the far-infrared laser interferometer, which are profile measurement diagnostics for the electron temperature, the soft x-ray emission, and the electron density, respectively. In this plasma, a continuous (2, 1) mode is excited after a deuterium pellet injection into a Ohmic plasma with $q_a = 5.8$. Since a (1, 1) mode is not observed, the rotational tomography of the soft x-ray and the electron density is possible. The island structure in the ECE image is not clear, because the electron temperature profile is hollow from the center to the island. The island structure in the density tomography is not so clear as the soft x-ray tomography, because the spatial resolution of the density measurement is relatively poor. Since the electron temperature is slightly hollow, the soft x-ray emission profile represents the plasma density profile. The size and position of the observed island from these different diagnostics is similar, and the result shows that both the particle diffusion and the heat conduction are fast inside the island. Comparing the ECE image and the soft x-ray tomography, it is found that the temperature at the O-point is higher than at the X-point. Therefore, in the plasma with the hollow temperature profile, the ECE signals is high at the O-point (time A) and low at the X-point (time B), as shown in Fig. 4(a). Of course, in the plasma with the peaked temperature profile, the ECE signals is high at the X-point (time A) and low at the O-point (time B), as shown in Fig. 5(a).

C. (2, 1) mode in pellet fueled plasma

An example of a (2, 1) mode in a deuterium pellet fueled Ohmic plasma is shown in Figs. 5 and 6. The (2, 1) mode appears after a relaxation event during the reheat period fol-
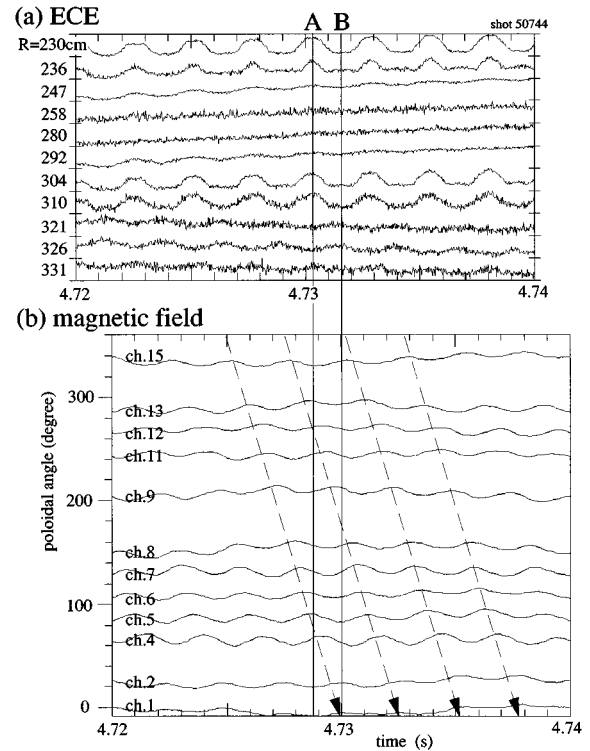

FIG. 4. (a) ECE signals showing the (2, 1) mode in the Ohmic plasma with deuterium pellet injection. (b) Wave forms of magnetic field (time integral of the magnetic fluctuation signal) which is measured by the Mirnov coil system.

lowing injection of a pellet. The detail of the relaxation will be presented in Sec. V. The soft x-ray and ECE signals are shown in Fig. 5. Since the (1, 1) mode does not exist in the core region, the soft x-ray signal shows a clear (2, 1) mode. In the soft x-ray signals, the phase inversion is seen at $p = 9$ cm, while in the ECE signals, the phase inversion is seen at $p = 38$ cm, where p is the radius of the x-ray chord from the magnetic axis. Therefore, it is hard to determine the radius of the phase inversion from the soft x-ray signals. Compared with the ECE signal, soft x-ray (2, 1) signals at the outer channel ($p = -32$ to -21 cm) are slightly mixed with a triangular wave, which comes from the (3, 1) mode. Since the ECE is a local measurement, it shows each mode separately.

Figure 6 shows contour plots of the ECE image reconstruction and the soft x-ray tomography of the (2, 1) island structure. Soft x-ray tomography shows an elliptical island in the core region indicating that the soft x-ray emission in the island is low and the island is crescent-shaped. The position and shape of the island indicated by soft x-ray tomography is consistent with the ECE reconstruction. The (2, 1) island structure is not clear in the soft x-ray tomography since the pellet fueled plasma has an extremely peaked density profile, and the low energy soft x-ray photon from the low temperature region is cut off by the thick beryllium foil. The ECE image reconstruction provides a clear picture of the (2, 1) island structure, which is crescent-shaped as expected from the MHD theory. The contour plot of the ECE (perturbation) shows clear boundary between the positive and negative per-
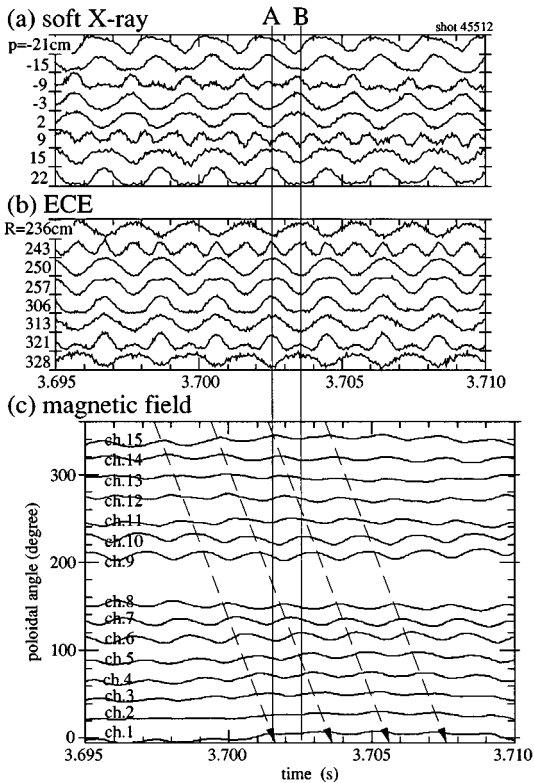
FIG. 5. (a) Soft x-ray and (b) ECE signals showing the (2, 1) mode in the Ohmic plasma with deuterium pellet injection. (c) Wave forms of magnetic field (time integral of the magnetic fluctuation signal) which is measured by the Mirnov coil system.

turbation (Fig. 6). This result is identical to the theoretical prediction as stated in the previous section (Sec. III A).

The frequency of the ECE signal at the phase inversion ($R = 243$, 321 cm) is double the other ECE signals. Consis-
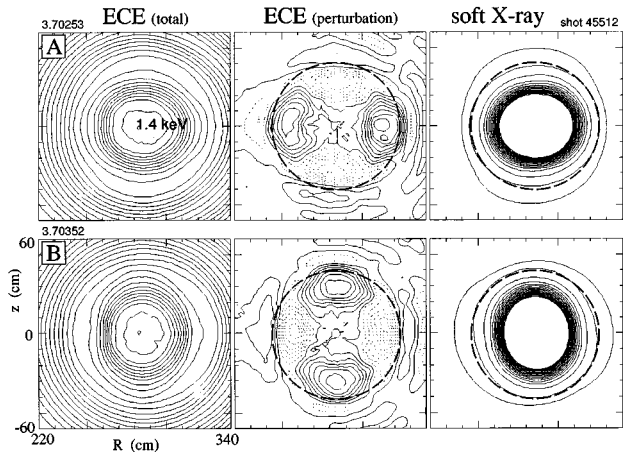

FIG. 6. Contour plot of electron temperature profile [ECE(total)], the perturbation on the temperature [ECE(perturbation)], and the soft x-ray tomography (soft x-ray) of the (2, 1) mode in the Ohmic plasma with deuterium pellet injection. The contour step size is 60 eV for the ECE(total), 8 eV for ECE(perturbation). The dotted contour indicate negative value. In the soft x-ray tomography, only 1/6 of peak emission is shown and the contour step size is 1/120 of the peak emission. The numbers on the left shoulder of the figures indicate the reconstruction time in seconds. The capital letters on the left of the figures correspond to the alphabets in Fig. 5. The broken circular line indicates the estimated $q = 2$ surface.
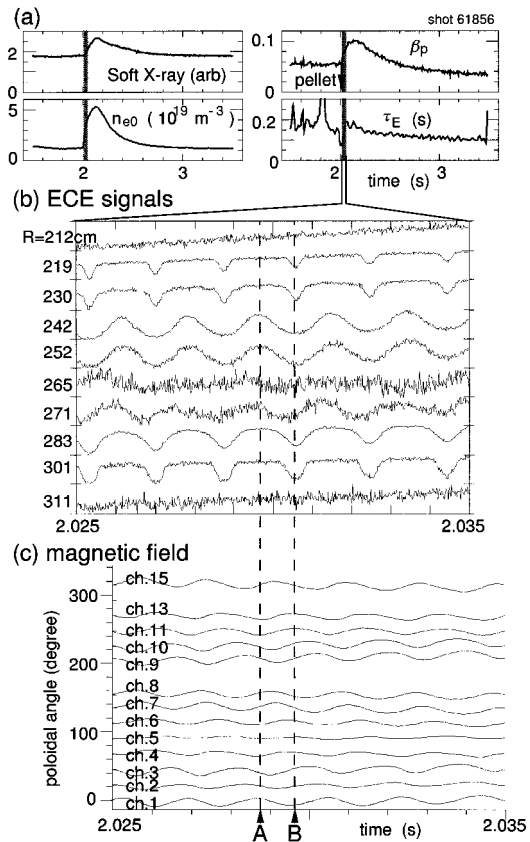

FIG. 7. (a) Time evolution of soft x-ray, central plasma density (n_{e0}), poloidal beta (β_p), and energy confinement time (τ_E) in the case of the lithium pellet injection. (b) ECE signals showing the (2, 1) mode in the Ohmic plasma with lithium pellet injection. (c) Wave forms of magnetic field (time integral of the magnetic fluctuation signal).

tent with this frequency doubling, the temperature at the O-point of the island is higher than the region between the X-point and the O-point. In the ECE image reconstruction (Fig. 6), a bulge is seen near the O-point. However, this may be due to the poor resolution of the ECE diagnostics, because the frequency doubling is not observed in the inner channels ($R = 250$, 313 cm in Fig. 5). Probably, this frequency doubling indicates that the temperature at the O-point is higher than the other part of the island.

D. (2, 1) mode in the lithium pellet injected plasma

An example of a (2, 1) mode in a lithium pellet fueled Ohmic plasma is shown in Figs. 7–9. Figure 7(a) shows the time evolution of soft x-ray emission, n_{e0}, β_p, and τ_E. A lithium pellet is injected into the Ohmic plasma with $q_a = 6$ at $t = 2$ s. The ECE signals and the magnetic field after the lithium pellet injection are shown in Figs. 7(b) and (c), respectively. The (2, 1) mode grows after the pellet injection. The ECE signals are shown in Fig. 7(b). A significant feature of this (2, 1) mode is that the wave form of the ECE signal has a dip at the O-point (time B). This is opposite to the case of the deuterium pellet injected plasma (cf. Fig. 5). The ECE reconstruction and soft x-ray tomography are shown in Fig. 8. Figure 9 shows the detail of the island structure at time B.
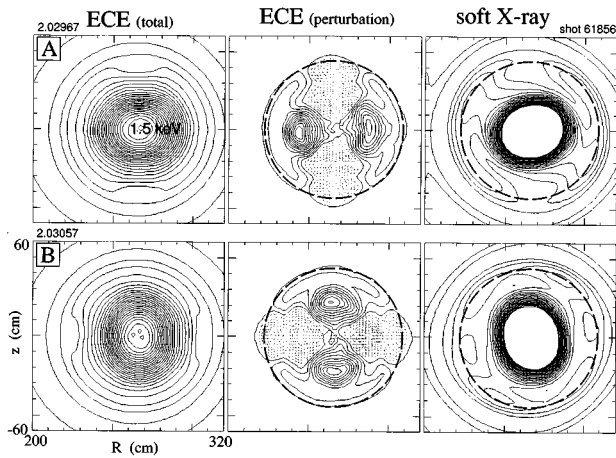
FIG. 8. Contour plot of electron temperature profile [ECE(total)], the perturbation on the temperature [ECE(perturbation)], and the soft x-ray tomography (soft x-ray), of the (2, 1) mode in the Ohmic plasma with lithium pellet injection. The contour step size is 60 eV for the ECE(total), 10 eV for ECE(perturbation). In the soft x-ray tomography, only 1/6 of peak emission is shown and the contour step size is 1/120 of the peak emission. The numbers on the left shoulder of the figures indicate the reconstruction time in seconds. The capital letters on the left of the figures correspond to the alphabets in Fig. 7. The broken circular line indicates the estimated $q = 2$ surface.

The (2, 1) island shape is elliptic, which is different from the normal (2, 1) island shape (cf. Figs. 6 and 10). This isolated island structure suggests that the island is made of own flux surfaces isolated from the main flux surface as is expected by the MHD theory.[2] The radial structure of the perturbation is different from the normal (2, 1) mode (cf. Figs. 6 and 10). In the contour plot of the ECE (perturbation), the negative perturbation is not seen outside the O-point. The island shape is similar to that seen during the snake oscillation.[19] The electron temperature at the O-point is lower than that at the X-point. The soft x-ray emissivity at the O-point is also
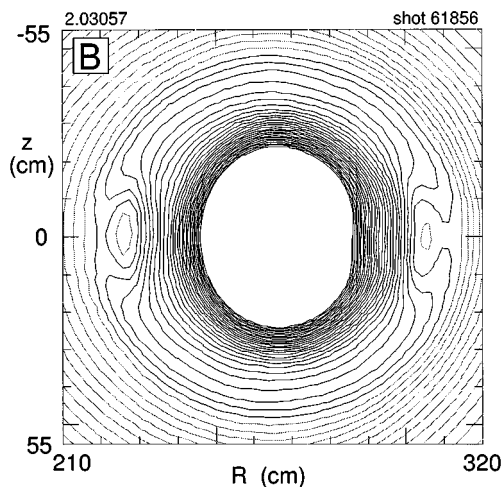

FIG. 9. Contour plot of electron temperature profile showing the (2, 1) mode in the Ohmic plasma with lithium pellet injection. The contour step size is 20 eV, and the dotted contour shows the temperature less than 30 eV. The saturation level is 800 eV, which is a half of the peak value.
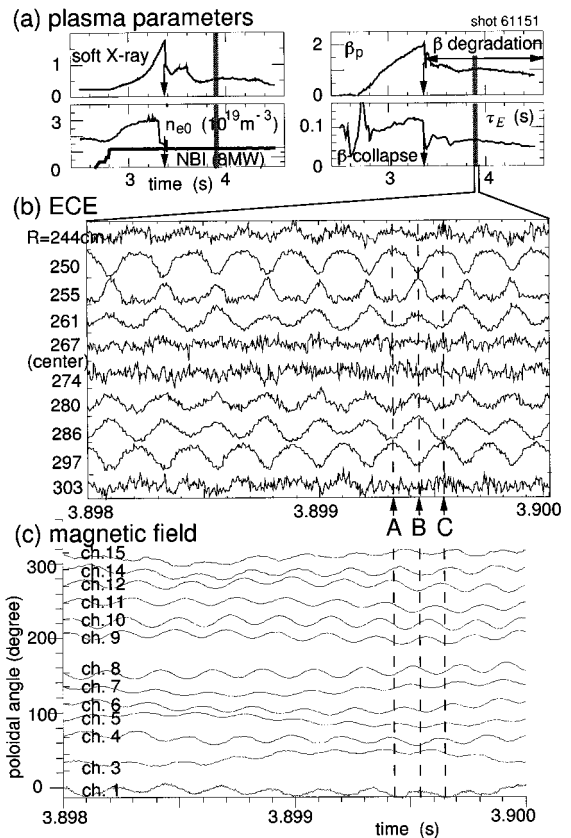

FIG. 10. (a) Time evolution of soft x-ray, central plasma density (n_{e0}), poloidal beta (β_p), and energy confinement time (τ_E) in high q plasma ($q_a = 16$). (b) ECE signals of the (2, 1) mode after the β collapse. (c) Wave forms of magnetic field (time integral of the magnetic fluctuation signal).

lower than that at the X-point. Therefore the density at the O-point may not be higher. This is different from the normal snake oscillation.[19]

E. (2, 1) mode after the beta collapse

After the β collapse, a strong MHD mode is enhanced, and the confinement time deteriorates noticeably. This phase is called the β degradation.[10,11] During the β degradation, no sawtooth is observed. In lower q plasmas ($q_a \sim 6$) the (3, 2) islands appears during the β degradation, the (2, 1) islands are more common in higher q plasmas ($q_a \sim 12$). An example of a (2,1) mode after the β collapse in the high q plasma (the cylindrical q_a is 16) is shown in Figs. 10 and 11. Figure 10(a) shows the time evolution of soft x-ray emission, n_{e0}, β_p, and τ_E. The β collapse takes place at $t = 3.38$ s. The ECE signals and the magnetic field during the β degradation phase are shown in Figs. 10(b) and (c), respectively. The phase velocity of the $m = 2$ wave on the bad curvature side (poloidal angle $\theta = 120° - 240°$) is slower than that on the good curvature side ($\theta = 0° - 120°$, and $240° - 360°$). This is an interesting feature in high β_p plasmas,[20] and is opposite in low β_p plasmas (cf. Figs. 5 and 7).

The ECE reconstruction of the electron temperature profile and the ECE perturbation profile are shown in Fig. 11. The island shape is crescent-shaped as in usual cases. The contour plot of the ECE (perturbation) shows clear boundary
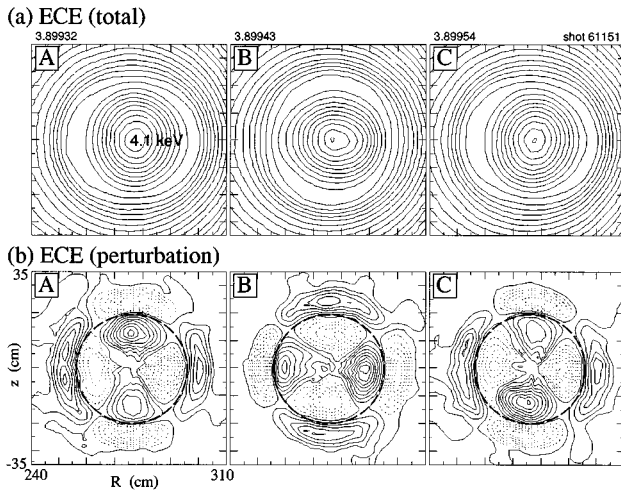
FIG. 11. (a) Contour plot of the electron temperature profile at the moment which is indicated by a capital letter on the left of the figure. The contour step size is 150 eV. The numbers on the left shoulder of the figures indicate the reconstruction time in seconds. (b) Reconstruction of the temperature difference. The contour step size is 15 eV and dotted lines indicate less than 300 eV. The broken circular line indicates the estimated $q=2$ surface.

between the positive and negative perturbation in the radial and the poloidal directions [Fig. 11(b)]. This is similar to the former case (cf. Fig. 6), but the perturbation outside of the rational surface is wider and stronger than the former case (cf. Fig. 6). A stronger hot spot perturbation is rotating. Probably, an unknown mode may overlap on the (2, 1) mode. The amplitude of the perturbation of the hot spot does not change when the hot spot is on the good or bad curvature side. Other examples of the (2, 1) mode shown in this paper also have
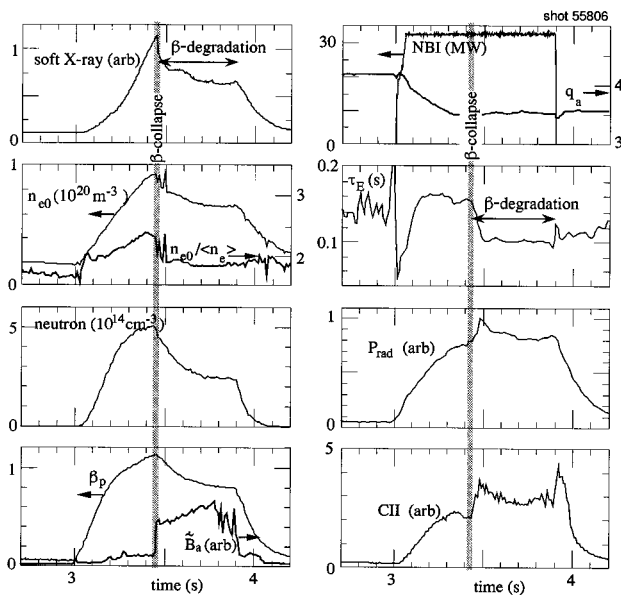

FIG. 12. Time evolution of soft x-ray, central plasma density (n_{e0}), density peaking parameter ($n_{e0}/\langle n_e \rangle$), total neutron count, poloidal beta (β_p), Mirnov coil signal ($\dot{\tilde{B}}_a$), NBI power, cylindrical q-value at edge (q_a), energy confinement time (τ_E), radiation power (P_{rad}) measured by a bolometer and CII emission in the case of the (3, 2) mode. An expansion of the moment that is indicated by an arrow is shown in Fig. 13.
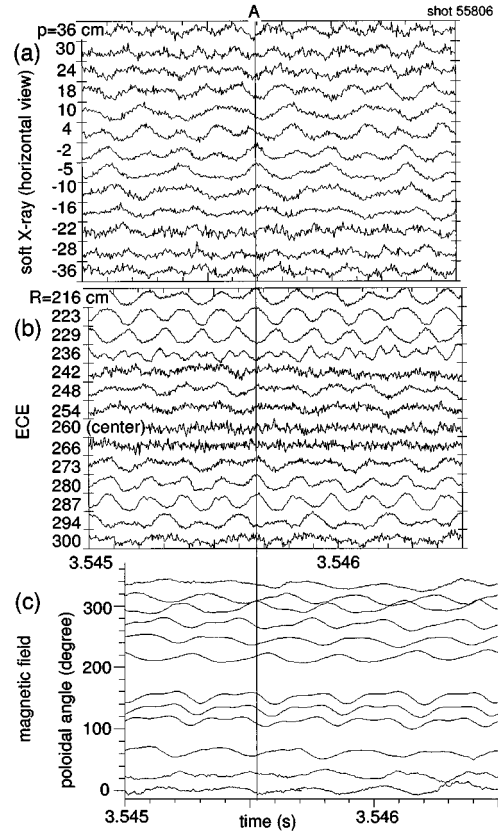

FIG. 13. ECE, soft x-ray and the poloidal magnetic field signals showing the (3, 2) mode after the β collapse.

this feature, which is remarkably different to the noticeable in–out asymmetry of the island structures of the (1, 1) mode[21] and the (3, 2) mode (cf. Fig. 14).

IV. (3, 2) MODE

A. (3, 2) mode after the beta collapse

A typical example of MHD activity during a β degradation is shown in Figs. 12–14. Figure 12 shows the Time evolution of soft x-ray, central plasma density (n_{e0}), density peaking parameter ($n_{e0}/\langle n_e \rangle$), total neutron count, poloidal beta (β_p), Mirnov coil signal ($\dot{\tilde{B}}_a$), NBI power, cylindrical q-value at edge (q_a), energy confinement time (τ_E), radiation power (P_{rad}) measured by a bolometer and CII emission. At $t=3.5$ s, a β collapse takes place, and the β_p and the τ_E drop significantly. The plasma has a major radius of 245 cm, minor radius of 80 cm, axial toroidal magnetic field of 4.8 T, and a plasma current of 1.9 MA. Before the collapse, this plasma had a central ion temperature of 30 keV, central electron temperature of 12 keV, $n_{e0}=1\times10^{20}$ m^{-3}, $n_{e0}/\langle n_e \rangle=2.4$. The soft x-ray, the ECE signals and the poloidal magnetic field during the β degradation phase are shown in Fig. 13. The fast oscillations are the (3, 2) mode. The slow oscillations on the interior channels are the (1, 1) mode. In the magnetic field, the $n=1$ mode is dominant, and the (3, 2) mode appears only on the outboard side.

The ECE image and soft x-ray tomography are shown in Fig. 14. In this example, island structures other than the (3,
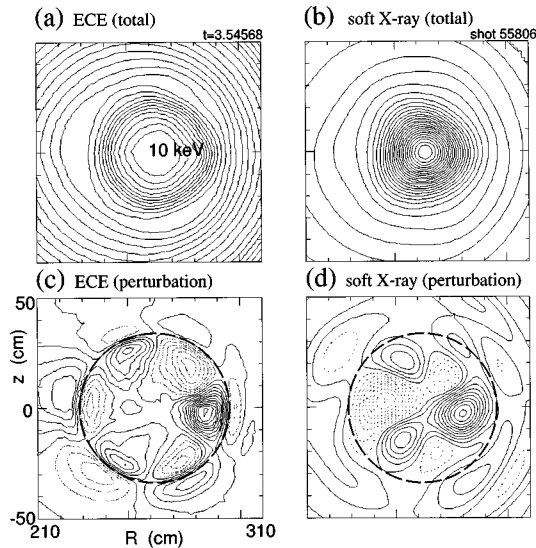
FIG. 14. (a) ECE image (contour plot of the electron temperature profile) at time B in Fig. 12. The contour step size is 400 eV. (b) Soft x-ray tomography. (c) Contour plot of the profile of the electron temperature perturbation, the contour step size is 40 eV. (d) Contour plot of the perturbation profile of the soft x-ray emissivity. The broken circular line indicates the phase inversion radius of (3, 2) mode. This circle can be assumed to be $q = 1.5$ surface.
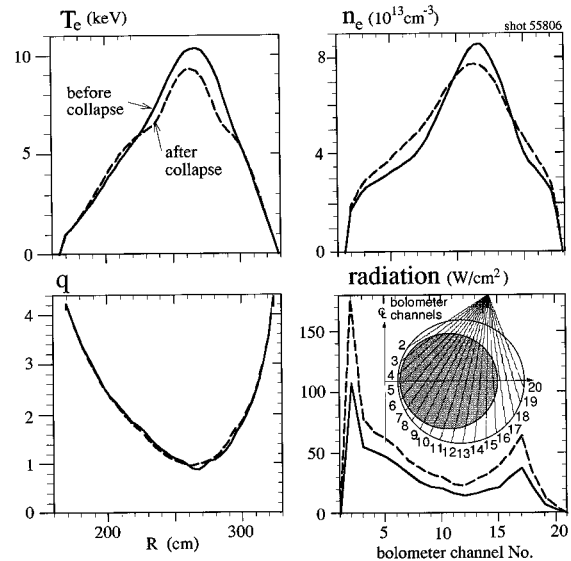

FIG. 15. Radial profiles of the electron temperature, the density, the q value and the radiation before and after the onset of the (3, 2) mode. The q-profile is estimated by the use of TRANSP.[22]

2) mode are not seen, and the mode mixing of the (1, 1) and (2, 1) modes is caused after the β collapse. The images of the perturbation are shown in Fig. 14. Here, the perturbation of the soft x-ray is the summation of the $m \geq 1$ components, which is the residual part after the subtraction of the symmetric part ($m = 0$ component). From the mode analysis of the Mirnov oscillation, the mode is identified as a (3, 2) mode. Therefore, the rational surface is the $q = 1.5$ surface. The island size on the weak field side is smaller than that on the strong field side due to the Shafranov shift. The amplitude of the perturbation is greater on the weak field side. The rational surface can be seen as a circle of zero perturbation in the perturbation image.

B. MHD effects on transport

On shot 55806 in Fig. 12, the β collapse takes place at $t = 3.45$ s (indicated by a hatched line). After the β collapse, the (3, 2) mode is enhanced and the energy confinement time drops significantly. Figure 15 shows radial profiles of the electron temperature, the electron density, and the evaluated q-profile before and after the onset of the (3, 2) mode. The q-profile is estimated from the time resolved profile measurements of temperature, density, and radiation using the 1.5-D transport analysis code TRANSP.[22] The electron heat conduction profile estimated with TRANSP is shown in Fig. 16. It is seen that the heat conduction at the (3, 2) island is three times higher than that without (3, 2) mode, as is assumed by Chang and Callen in their model for the confinement degradation due to the island.[23] This result shows that the large amplitude MHD mode enhances the heat conduction. In this case, however, the confinement time degradation is greater than the theoretical model. This may be because the MHD activity enhances both the loss of fast ions and the

radiation loss. The radiation loss increases 50% after the β collapse on shot 55806 (Fig. 15). The (3, 2) island may also enhance the plasma–wall interaction.

V. RELAXATION DUE TO (2, 1) MODE

An example of the relaxation in a deuterium pellet fueled Ohmic plasma is shown in Figs. 17–19. Figure 17 shows the time evolution of soft x-ray emission, n_{e0}, $n_{e0}/\langle n_e \rangle$, Mirnov coil signal ($\dot{\tilde{B}}_a$), β_p, and τ_E. A three-dimensional (3-D) plot of the time evolution of the electron temperature profile is shown in Fig. 18. A deuterium pellet is injected into the Ohmic plasma with $I_p = 1.2$ MA and $q_a = 3.8$. The plasma major radius is 270 cm and the minor radius is 88 cm. In this case, the pellet deeply penetrates into the plasma, and the central temperature drops significantly causing a hollow temperature profile. The (2, 1) mode grows
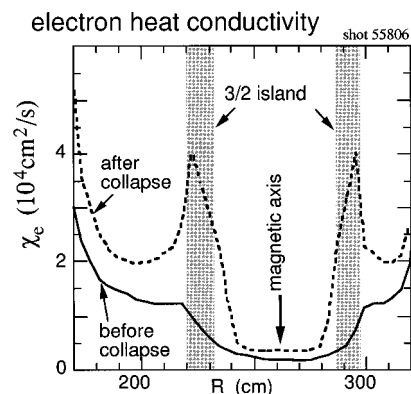

FIG. 16. Radial profile of electron heat conduction rate which is calculated with the transport code TRANSP before ($t = 3.38$ s) and after ($t = 3.54$ s) the onset of the (3, 2) mode. The hatched area indicates the (3, 2) island region.

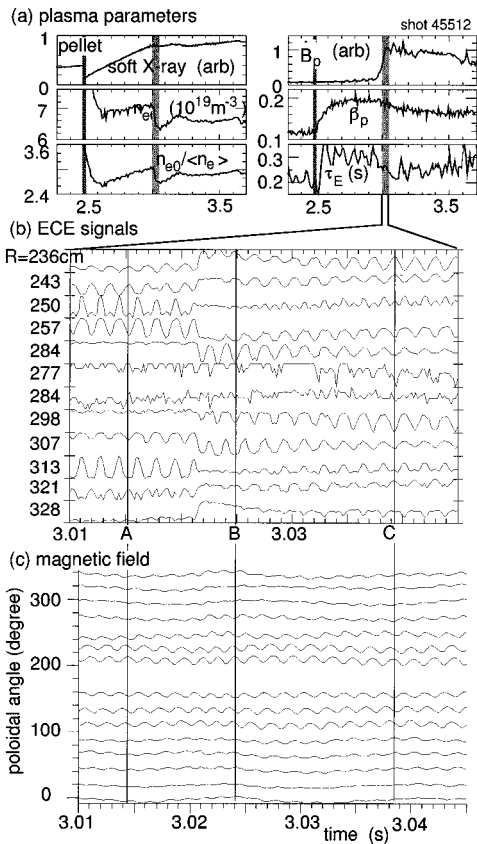Phys. Plasmas, Vol. 3, No. 7, July 1996

Nagayama *et al.* 2637

FIG. 17. (a) Time evolution of soft x-ray, central plasma density (n_{e0}), density peaking parameter ($n_{e0}/\langle n_e \rangle$), Mirnov coil signal ($\dot{\tilde{B}}_p$), NBI power, cylindrical q-value at edge, poloidal beta (β_p), and energy confinement time (τ_E). (b) ECE signals in the case of relaxation due to (2, 1) mode. (c) The poloidal magnetic field.

for 0.5 s after the pellet injection. Due to the relaxation, the electron temperature profile is changed from a broad profile to a peaked one.

In the Fig. 17(a), it is seen that the soft x-ray intensity grows linearly after the pellet injection, and saturates at $t=3$ s, when the central electron density drops. At the same time,
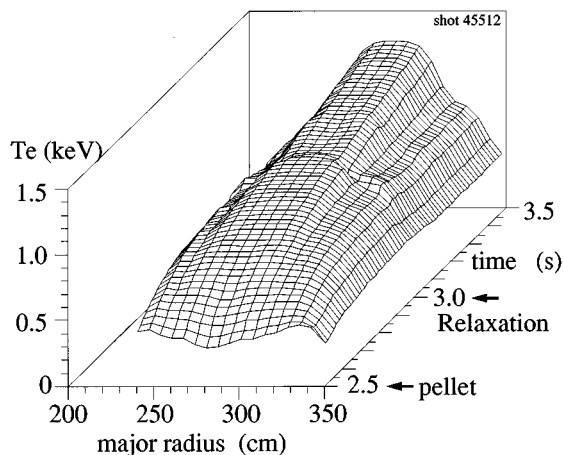

FIG. 18. Time evolution of electron temperature profile after the deuterium pellet injection.
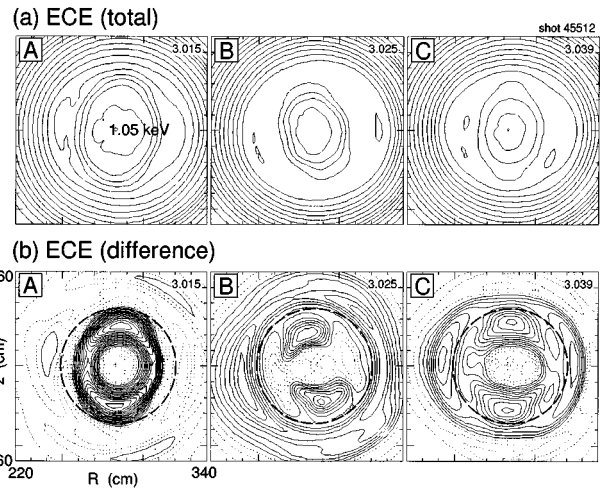

FIG. 19. (a) Contour plot of the electron temperature profiles before (frame A) and after (frame B) the relaxation. The capital letters on the left of the figures correspond to the alphabets in Fig. 17. The contour step size is 60 eV. (b) Contour plot of the electron temperature difference. The contour step size is 10 eV and dotted lines indicate less than 50 eV. The broken circular line indicates the $q=2$ surface, which is estimated from the contour plot of the ECE perturbation.

both β_p and τ_E decrease, in a manner similar to a β collapse. In the ECE signals, a relaxation is observed at $t=3.02$ s (see Fig. 18). The ECE signals for the case of a relaxation due to a (2, 1) mode is shown in Fig. 17(b). The ECE reconstruction before and after the relaxation are shown in Fig. 19. Here the temperature difference $\Delta T_e(r,\theta)$ is defined as

$$\Delta T_e(r,\theta) = T_e(r,\theta) - Min[T_e(r,\theta)], \qquad (2)$$

where $Min[T_e(r,\theta)]$ is the minimum over a full time interval of the crash phase. The temperature difference shows how the heat is transported from the inside of the inversion radius to the outside.[24] The (2, 1) island becomes a flat ring during the relaxation. After the crash, a clear heat ring is established outside of the $q=2$ surface. This indicates that the heat in the interior region of the $q=1$ surface moves to the outer region of the $q=2$ surface. Therefore, the field lines inside and outside of the $q=2$ surface are connected. This phenomenon is similar to the partial sawtooth crash.[25,26]

The full sawtooth crash used to be explained by the full reconnection model,[27] and it may be possible in the case of the (1, 1) mode. However, the full reconnection at the X-point of the island does not make a flat ring but makes the (2, 1) island wider. Therefore the above relaxation phenomenon cannot be explained by a full reconnection. The similar partial collapse of the soft x-ray profile has been observed during the minor disruption.[6,28] In that case, since the fast growing (3, 2) mode was observed as a precursor of the partial collapse, the stochastic field line due to the overlapping of (3, 2) mode and (2, 1) mode was considered to cause the partial collapse. Another possible mechanism is the localized reconnection at the X-point,[29] which is useful to explain the sawtooth crash without great change of q-profile before and after the crash.[21] Suppose the local pressure steepening that arises from the evolution of the (2, 1) mode causes a MHD instability at the X-point in the bad curvature

Nagayama *et al.*

side; this instability enhances the reconnection locally. Since one flux surface is made of one field line nests, all particles and heat can quickly escape along the reconnected field line through the localized portion. During this process the magnetic island structure does not disappear. The remaining (2, 1) mode after the relaxation [Fig. 19[B]] is consistent with this speculation. Another possible mechanism of the relaxation is that the newly enhanced instability overlaps to the (2, 1) mode and causes the stochastic field line. Since this process is also a local phenomenon, the result of this process is similar to that of the localized reconnection process.

VI. MIRNOV OSCILLATION AND OBSERVED ISLAND

A magnetic pick up coil array (Mirnov coil[1]) is an established diagnostic for the MHD mode structure. The sinusoidal oscillation of the magnetic field is normally interpreted as a rotation of the (2, 1) island structure. Now, we can measure the island structure of the (2, 1) mode to compare the island structure and the Mirnov coil signals. Figure 4 shows the ECE signals and the magnetic field, which is a time integral of the magnetic fluctuation signal being measured by the Mirnov coil system on the inside of the vacuum vessel. The origin of the poloidal angle is on the inner midplane, so that the top of the plasma is at 90°. The capital letters correspond to those on the left of the contour plot in Fig. 3. As shown in Fig. 1, the toroidal angle between the Mirnov coil system and the ECE system is 189° in the direction of the mode rotation. To compensate for the phase difference between the ECE and magnetic field signals, the data are shifted by 2.7 ms since the period of one cycle of the (2, 1) mode is 5.1 ms. At time A, the maximum magnetic field is at the top and the bottom, where the X-point of the (2, 1) island is. At time B, the minimum magnetic field is on the mid-plane, where the O-point of the (2, 1) island is located.

Another example is plotted in Fig. 5, which shows the soft x-ray signals, the ECE signals and the magnetic field from the Mirnov coil system. To compensate for the phase difference between the ECE and magnetic field signals, the data are shifted by 1 ms since a period of one cycle of the (2, 1) mode is 2 ms. The capital letters correspond to those on the left of the contour plots in Fig. 6. At time A, the maximum magnetic field is on the mid-plane, where the X-point of the (2, 1) island is. At time B, the minimum magnetic field is at the top and the bottom, where the O-point of the (2, 1) island is located. In all cases presented in this paper, the magnetic field is maximum at the X-point (cf. Figs. 4, 5, 7, 10, 13, 17).

An estimate of the island width (w) may be obtained from the Mirnov coil signal using the relation[2,3]

$$w \approx 4r \left(\frac{B_r^1}{m B_\theta} \left| \frac{q}{rq'(r)} \right| \right)^{1/2}, \qquad (3)$$

where r_s is the radius of the mode rational surface, m is the poloidal mode number, B_r^1 is the radial field perturbation, and q' is the radial derivative of q. The island size is wider when the Mirnov coil signal amplitude is larger. Figure 20 shows that the comparison of the island widths obtained by the ECE imaging versus those estimated from the Mirnov
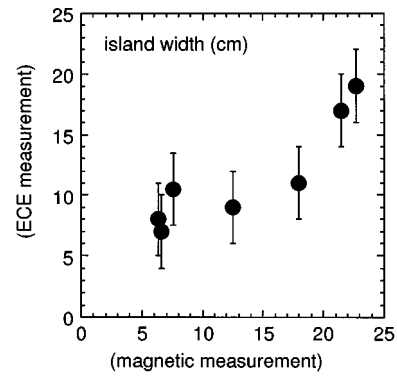

FIG. 20. Comparison of the island widths obtained by the ECE imaging versus those estimated using the Mirnov coil signal and the transport code SNAP that estimates the q profile from the measured temperature, density and impurity profiles and the other diagnostics data.

coil signal using the q-profile estimated from the SNAP code, which uses the profile measurements of temperature, density and radiation. The data are randomly sampled. The error of the ECE measurement is 3 cm, which is a half of the channel separation. The magnetic measurement provides a comparable island width. The experiment suggests that Mirnov oscillation is generated by the island rotation.

However, when the temperature profile is flat and the magnetic island is far from the plasma edge, the magnetic field is weak and the estimation error is large. Figure 21 shows the ECE image of the (2, 1) island structures after the
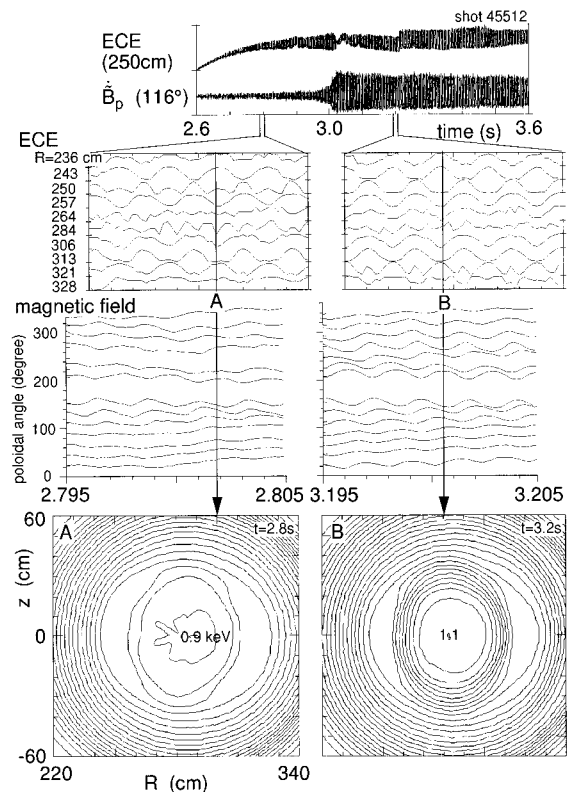

FIG. 21. ECE and magnetic signals, and contour plot of electron temperature profile.

Phys. Plasmas, Vol. 3, No. 7, July 1996

Nagayama *et al.*   2639

pellet injection. The temperature profile is flat at time A, and is peaked at time B. The amplitude of the magnetic field fluctuation is very different, but the island size is similar. At time A, the (2, 1) mode is not dominant in the magnetic signals. The island width on the ECE reconstruction is much wider than the estimation by Eq. (3). At $t=3$ s the (2, 1) mode signal quickly grows. At time B, the (2, 1) mode is dominant in the magnetic signals. This phenomena is interesting, but the q-profile is necessary for the further discussion, while unfortunately the q-profile in Ohmic plasmas cannot be measured on TFTR.

VII. SUMMARY

Using the ECE image reconstruction technique, we have observed the (2, 1) and (3, 2) islands are crescent-shaped as expected by the MHD theory. We have also observed a cold elliptic island with closed surfaces, which occurs after lithium pellet injection. The first attempt of a comparison between the observed island and the Mirnov oscillation has been done. It has been observed that the magnetic field is maximum at the X-point. The results have suggested that the Mirnov oscillation is generated by the island rotation. The phenomenon related to the (2, 1) or (3, 2) island have been also presented here. We have obtained evidence for the enhanced heat transfer due to the existence of the island. An interesting observation is the temperature profile relaxation due to the (2, 1) mode in Ohmic plasmas. The (2, 1) island becomes a flat ring, and the heat inside the $q=2$ surface is transferred to the region outside. The relaxation is not explained by the full reconnection. A possible mechanism is the localized reconnection or the stochasticity at the X-point, which is also a local phenomenon.

ACKNOWLEDGMENTS

[1] S. V. Mirnov and I. B. Semenov, Sov. J. Atomic Energy **30,** 22 (1971).

[2] G. Bateman, *MHD instabilities* (MIT Press, Cambridge, 1978).

[3] J. Wesson, *Tokamaks* (Oxford University Press, Oxford, 1987).

[4] N. R. Sauthoff, S. von Goeler, and W. Stodiek, Nucl. Fusion **18**, 1445 (1978); N. R. Sauthoff and S. von Goeler, IEEE Trans. Plasma Sci. **PS-7**, 141 (1979).

[5] Y. Nagayama, S. Tsuji, K. Kawahata, N. Noda, and S. Tanahashi, Jpn. J. Appl. Phys. **20**, L779 (1981).

[6] S. Tsuji, Y. Nagayama, K. Miyamoto, K. Kawahata, N. Noda, and S. Tanahashi, Nucl. Fusion **25**, 305 (1985).

[7] Y. Nagayama, R. Büchse, A. Cavallo, E. Fredrickson, A. Janos, K. McGuire, J. Kuo Petravic, C. Sule, and G. Taylor, Rev. Sci. Instrum. **61**, 3265 (1990).

[8] Y. Nagayama, K. M. McGuire, M. Bitter, A. Cavallo, E. D. Fredrickson, K. W. Hill, H. Hsuan, A. Janos, W. Park, G. Taylor, and M. Yamada, Phys. Rev. Lett. **67**, 3527 (1991).

[9] Y. Nagayama, Rev. Sci. Instrum. **65**, 3415 (1994).

[10] Y. Nagayama, S. A. Sabbagh, J. Manickam, E. D. Fredrickson, M. Bell, R. V. Budny, A. Cavallo, A. C. Janos, M. E. Mauel, K. M. McGuire, G. A. Navratil, G. Taylor, and M. Yamada, Phys. Rev. Lett. **69**, 2376 (1992).

[11] Y. Nagayama, M. Yamada, S. A. Sabbagh, J. Manickam, E. D. Fredrickson, M. Bell, R. V. Budny, A. Cavallo, A. C. Janos, M. E. Mauel, K. M. McGuire, G. A. Navratil, and G. Taylor, Phys. Fluids B **5**, 2571 (1993).

[12] A. Cavallo, R. C. Cutler, and M. P. McCarthy, Rev. Sci. Instrum. **59**, 889 (1988).

[13] F. J. Stauffer, D. A. Boyd, R. C. Cutler, M. Diesso, M. P. McCarthy, J. Montague, and R. Roco, Rev. Sci. Instrum. **59**, 2139 (1988).

[14] K. W. Hill, S. Von Goeler, M. Bitter, W. Davis, L. Dudek, E. Fress, L. C. Johnson, J. Kiraly, K. McGuire, J. Montague, E. Moshey, N. R. Sauthoff, and K. M. Young, Rev. Sci. Instrum. **56**, 830 (1985); J. Kiraly, M. Bitter, P. Efthimion, S. Von Goeler, B. Grek, K. W. Hill, D. Johnson, K. McGuire, N. R. Sauthoff, S. Sesnic, G. Tait, and G. Taylor, Nucl. Fusion **27**, 397 (1987).

[15] L. C. Johnson, M. Bitter, R. Chouinard, S. Von Goeler, K. W. Hill, S.-L., Liew, K. McGuire, V. Pare, N. R. Sauthoff, and K. M. Young, Rev. Sci. Instrum. **57**, 2133 (1986).

[16] Y. Nagayama, J. Appl. Phys. **62**, 2702 (1987).

[17] D. K. Mansfield, H. K. Park, L. C. Johnson, H. M. Anderson, R. Chouinard, V. S. Foote, C. H. Ma, and B. J. Clifton, Appl. Opt. **26**, 4469 (1987).

[18] M. Zarnstorff, M. Bell, M. Bitter, C. Bush, E. Fredrickson, B. Grek, K. Hill, B. Howell, K. Jaehnig, D. Johnson, R. Knize, K. McGuire, A. Ramsey, G. Schilling, J. Schivell, S. Scott, and G. Taylor, in *Proceedings of the 15th European Conference on Controlled Fusion and Plasma Physics*, Dubrovnik, 1988 (European Physical Society, Petit-Lancy, Switzerland, 1988), Vol. 1, p. 95.

[19] A. Weller, A. D. Cheetham, A. W. Edwards, R. D. Gill, A. Gondhalekar, R. S. Granetz, J. Snipes, and J. A. Wesson, Phys. Rev. Lett. **59**, 2303 (1987); Y. Nagayama and A. W. Edwards, Rev. Sci. Instrum. **63**, 4757 (1992).

[20] G. Fussmann, B. J. Green, and H. P. Zehrfeld, in *Plasma Physics and Controlled Nuclear Fusion Research*, Brussels, 1980 (International Atomic Energy Agency, Vienna, 1981), Vol. 1, p. 353.

[21] Y. Nagayama, M. Yamada, W. Park, E. D. Fredrickson, A. C. Janos, K. M. McGuire, and G. Taylor, Phys. Plasmas **3**, 1647 (1996).

[22] R. J. Hawryluk, in *Physics of Plasma Close to Thermonuclear Conditions*, edited by B. Coppi, G. G. Leotta, D. Pfirsch, R. Pozzoli, and E. Sindoni (Commission of the European Communities, Brussels, 1980), Vol. 1, p. 19.

[23] Z. Chang and J. D. Callen, Nucl. Fusion **30**, 219 (1990).

[24] M. Yamada, Y. Nagayama, W. Davis, E. Fredrickson, A. Janos, and F. Levinton, Rev. Sci. Instrum. **63**, 4623 (1992).

[25] V. V. Parail and G. V. Pereverzev, Fiz. Plasmy **6**, 27 (1980) [Sov. J. Plasma Phys. **6**, 14 (1980)].

[26] Y. Nagayama, G. Taylor, M. Yamada, E. D. Fredrickson, A. C. Janos, and K. M. McGuire, Nucl. Fusion **36**, 521 (1996).

[27] B. B. Kadomtsev, Fiz. Plazmy **1**, 710 (1975) [Sov. J. Plasma Phys. **1**, 389 (1975)].

[28] Y. Nagayama, S. Tsuji, K. Miyamoto, K. Kawahata, N. Noda, S. Tanahashi, and J. Fujita, in *Plasma Physics and Controlled Nuclear Fusion Research*, Nice, 1988 (International Atomic Energy Agency, Vienna, 1989), Vol. 1, p. 387.

[29] Y. Nagayama, "Localized reconnection model for sawtooth crash," submitted to J. Plasma Fusion Res. (in Japanese).